

Multi-Messenger Insights into Ultra-High-Energy Cosmic Rays from FR0 Radio Galaxies: Emission Spectrum, Composition, and Secondary Photons and Neutrinos

Jon Paul Lundquist,^{a,*} Serguei Vorobiov,^a Lukas Merten,^{b,c} Anita Reimer,^d Margot Boughelilba,^d Paolo Da Vela,^d Fabrizio Tavecchio,^e Giacomo Bonoli^e and Chiara Righi^e

^aCenter for Astrophysics and Cosmology (CAC), University of Nova Gorica, Nova Gorica, Slovenia

^bInstitute for Theoretical Physics IV, Faculty for Physics and Astronomy, Ruhr University Bochum, Universitätsstraße 150, 44801 Bochum, Germany

^cRuhr Astroparticle and Plasma Physics Center (RAPP Center), Bochum, Germany

^dUniversität Innsbruck, Institut für Astro- und Teilchenphysik, Technikerstraße 25, 6020 Innsbruck, Austria

^eAstronomical Observatory of Brera, Via Brera 28, 20121 Milano, Italy

E-mail: jlundquist@ung.si

Despite their low individual luminosity, Fanaroff-Riley Type 0 (FR0) radio galaxies have emerged as potentially significant contributors to the observed flux of ultra-high-energy cosmic rays (UHECRs, $E \geq 10^{18}$ eV) due to their substantial prevalence in the local universe. Outnumbering more powerful FR radio galaxies by approximately fivefold within redshifts of $z \leq 0.05$, FR0s may contribute a considerable fraction of the total UHECR energy density. The presented comprehensive study employs CRPropa3 simulations to estimate the mass composition and energy spectra of UHECRs emitted by FR0 galaxies. These simulations, which integrate extrapolated FR0 properties and various configurations of intergalactic magnetic fields (both random and structured), are compared to recent data from the Pierre Auger Observatory using three extensive air-shower models. By fitting the simulated spectral indices, rigidity cutoffs, and elemental fractions to Auger's observed energy spectrum and $\langle \ln A \rangle$ composition, we probe the contribution of FR0 sources to the UHECR flux. Furthermore, we predict the secondary photon and neutrino fluxes resulting from UHECR interactions with cosmic photon backgrounds and compare these results with current upper limits and theoretical models. This multi-messenger approach provides valuable insights into the role of low-luminosity FR0 radio galaxies within the UHECR landscape.

*7th International Symposium on Ultra High Energy Cosmic Rays (UHECR2024)
17-21 November 2024
Malargüe, Mendoza, Argentina*

*Speaker

1. Introduction

Ultra-high-energy cosmic rays (UHECRs) are the universe's most energetic particles, yet their origins remain uncertain. Potential sources include active galactic nuclei, radio galaxies, gamma-ray bursts, and starburst galaxies. The Pierre Auger Observatory (Auger), the largest hybrid UHECR detector [1], measures their energy spectrum, mass composition, and arrival directions.

Fanaroff-Riley Type 0 (FR0) radio galaxies are promising UHECR sources: they outnumber FR1/2 galaxies fivefold within $z \leq 0.05$ [2]. Despite weak extended radio emission, FR0 jets can accelerate UHECRs via hybrid shear mechanisms[3], meeting both the Hillas [4] and energetics criteria [5]. Their low gamma-ray and neutrino emissions further support this role [6, 7].

In the full study [8] we investigate FR0s as UHECR sources using simulations that incorporate FR0 properties and intergalactic magnetic fields (IGMF). By fitting the simulated UHECR spectrum and composition to public Auger data, we assess FR0s' potential flux contribution and predict secondary photon and neutrino fluxes, providing a multi-messenger perspective on FR0s.

2. Simulating FR0s as UHECR Sources

UHECR propagation is simulated with CRPropa3 (v3.2) [9], accounting for all energy losses from cosmic photon background interactions and adiabatic expansion loss. Secondary neutrinos ($E > 100$ TeV) and photons ($E > 100$ MeV) are also tracked.

Propagation in four IGMF models and a no-field scenario were simulated (see [8] for field strength distributions). Two homogeneous turbulent fields with $\langle B \rangle = 1$ nG ($B_{\text{RMS}} = 1.1$ nG) follow a Kolmogorov spectrum with correlation lengths of 234 kpc (Rand.A) and 647 kpc (Rand.B). The Dolag et al. structured field [10] based on MHD simulations of primordial IGMF evolution, reproducing large-scale structures (e.g., Coma, Virgo, Centaurus), has $\langle B \rangle = 0.047$ nG, but strong local fields (up to ~ 10 μ G) yield $B_{\text{RMS}} = 11$ nG. The Hackstein et al. structured field (CLUES, 'astrophysical1R') [11], based on MHD simulation including gas cooling and AGN feedback, produces $\langle B \rangle = 0.064$ nG with $B_{\text{RMS}} = 1.2$ nG. Stronger filamentary fields connect clusters (e.g., Coma, Centaurus, Perseus), and a dipole anisotropy is observed for pure iron emission.

FR0 sources are upsampled from the FR0CAT catalog [2] ($z \leq 0.05$) within the $-45^\circ \leq \text{SGB} \leq 45^\circ$ and $60^\circ \leq \text{SGL} \leq 120^\circ$. These 76 FR0s are isotropically distributed which yields $\sim 18,400$ FR0s for a full-sky simulation extended to $z \leq 0.2$. The simulated FR0s match the redshift distribution, with UHECR flux proportional to radio luminosity, and redshift-flux correlation preserved to nonparametrically model source evolution [8]. Simulated FR0s emit UHECRs isotropically, consistent with their low-power jets and slow bulk flows, and the large number of random orientations.

Primaries emitted are H, He, N, Si, and Fe, approximating nuclear families that cover a broad range of species. Heavy elements beyond Fe are expected to be negligible. The mean logarithmic mass number ($\langle \ln A \rangle$) as a function of energy and initial spectrum are modified from emission to detection accounting for photon background interactions and radiative losses. The observed $\langle \ln A \rangle$ varies slightly with the fit spectral index γ , rigidity cutoff R_{cut} , and trajectory cutoff D_{cut} .

3. Fitting Composition and Energy Spectrum

The best-fit FR0 UHECR emission is determined by minimizing the $\Sigma \chi^2$ per degree of freedom for composition and energy spectrum using Auger data [12, 13]. Two emission fit approaches are used: an energy-independent composition and an evolving energy-dependent composition.

For the constant fraction fit, four parameters define the relative emitted nuclei fractions, constrained to sum to 100%. Remaining parameters include spectral index γ , rigidity-dependent cutoff R_{cut} [14], trajectory cutoff D_{cut} , and spectrum normalization n . The minimized cost function is $\sum \chi^2/N_{\text{dof}} = \sum \chi_E^2/N_{\text{dof}}^E + \sum \chi_C^2/N_{\text{dof}}^C$, where $N_{\text{dof}}^E = 8$ and $N_{\text{dof}}^C = 4$. $\text{Var}(\ln A)$ is not used due to negative values in QGS4 [12] and additional hadronic model uncertainties [15].

The evolving fraction fit follows a similar minimization but allows the emitted composition to vary with energy, resulting in 40 more parameters. This avoids the unphysical assumption of a constant emitted composition, capturing the effects of acceleration processes, spallation, and energy-dependent losses. However, it is an overfitting and is not a strong model discriminator.

Both fits are performed using SciPy's [16] Differential Evolution for global minimization, followed by deterministic fitting. The evolving fraction fit incrementally increases bin resolution, refining the energy dependence of the composition. Search ranges are: spectral index $-4.5 \leq \gamma \leq 4.5$, rigidity cutoff $10^{16} \leq R_{\text{cut}}/V \leq 10^{22}$, and trajectory cutoff $841 \leq D_{\text{cut}}/\text{Mpc} \leq 2000$. Confidence intervals are bootstrapped, incorporating all statistical and systematic data uncertainties.

4. Results

4.1 Constant Fraction Fit

The constant fraction fit results for all five magnetic field models and two EAS models (EPOS-LHC and Sibyll2.3c) are shown in Fig. 1, with QGSJetII-04 results provided in tables. The 1 nG random fields better fit the composition bins at the lowest energy. Only the Dolag and Rand.B models sufficiently account for the highest energy bin in the spectrum. The CLUES model does not contribute significantly to the last energy bin with $J(E) \cdot E^3 \sim 10^{33} \text{ eV}^2 \text{ km}^{-2} \text{ yr}^{-1} \text{ str}^{-1}$.

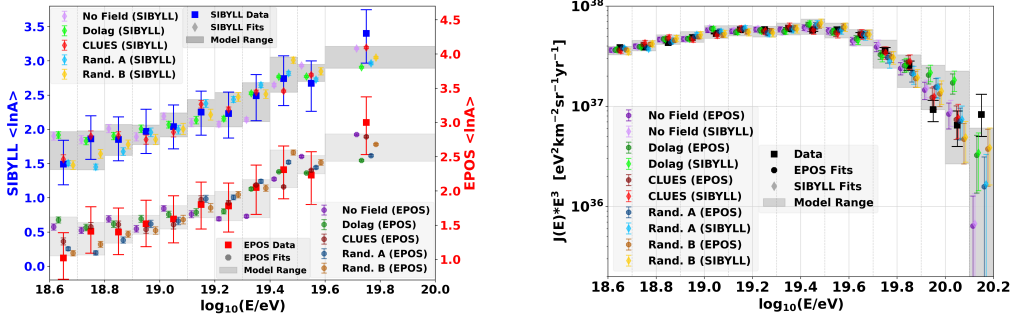


Figure 1: Constant fraction fit results. Offsets applied for visibility. Grey areas show $\pm 1\sigma$ bounds. Left: Mean log mass number $\langle \ln A \rangle$ (blue y-axis: SIBYLL, red: EPOS). Right: Energy spectra multiplied by E^3 .

Best-fit parameters and 1σ confidence intervals are given in Table 1 (for D_{cut} and n see [8]). CLUES-SIBYLL provides the best fit, followed by CLUES-EPOS. Excluding QGSJetII-04, Rand.B is the second-best magnetic field after CLUES. Weak-fields (no-field, Dolag) are disfavored, with all $\Sigma \chi^2 > 3$. QGSJetII-04 generally produces poorer fits, except when paired with random fields.

4.1.1 Energy Spectrum Parameters

The constant fraction energy spectrum parameters of Table 1 suggest that both magnetic field strength $\langle B \rangle$ and B_{RMS} influence the source emission spectrum. The spectral index γ decreases as $\langle B \rangle$ and B_{RMS} increase, with QGSJetII-04 producing harder spectra. The rigidity cutoff R_{cut} generally increases with $\langle B \rangle$ and B_{RMS} , though at low field strengths, it decreases with heavier

elemental composition. The trajectory cutoff D_{cut} and normalization n (see [8]) are generally stable.

Heavier composition models (Sibyll2.3c) result in softer spectra (higher γ), while QGSJetII-04 leads to the hardest emission spectra. Compared to previous FR0 fits limited to $z \leq 0.05$ [17], these results yield harder spectra and higher R_{cut} , except for Rand.B.

The exclusion of disfavored configurations (no-field, Dolag, CLUES-QGS4) results in best-fit ranges of $1.97 \leq \gamma \leq 2.54$ and $19.45 \leq \log_{10}(R_{\text{cut}}/V) \leq 19.86$. Compared to [18], these results align with their second-minima and $z < 0.02$ source distance fits.

4.1.2 UHECR Composition Parameters

Best-fit FR0 emission fractions are shown in Table 1. Due to propagation effects, a significant fraction of emitted helium converts to observed protons, leading to a degeneracy in proton vs. helium dominance. The total light fraction ($f_{\text{H}} + f_{\text{He}}$) remains more stable.

Field	Model	Spectrum Parameters			Nuclei Emission (%)					
		$\Sigma\chi^2/\text{dof}$	γ	$\log_{10}(R_{\text{cut}}/V)$	$f_{\text{H}} + f_{\text{He}}$	f_{H}	f_{He}	f_{N}	f_{Si}	f_{Fe}
No Field	SIBYLL	3.21	$2.51^{+0.02}_{-0.67}$	$19.36^{+0.23}_{-0.31}$	$88.7^{+0.2}_{-24.0}$	$88.7^{+0.1}_{-88.7}$	$0.0^{+16.5}_{-0.0}$	$0.0^{+23.1}_{-0.0}$	$6.1^{+6.8}_{-2.3}$	$5.2^{+2.0}_{-4.0}$
	EPOS	3.15	$2.50^{+0.02}_{-0.16}$	$19.40^{+0.13}_{-0.06}$	$93.4^{+0.7}_{-7.2}$	$93.4^{+0.6}_{-16.5}$	$0.0^{+12.1}_{-0.0}$	$0.0^{+5.8}_{-0.0}$	$2.9^{+2.4}_{-1.8}$	$3.7^{+0.8}_{-0.8}$
	QGS4	3.47	$2.47^{+0.03}_{-0.08}$	$19.43^{+0.10}_{-0.03}$	$97.6^{+0.3}_{-1.1}$	$97.6^{+0.1}_{-8.8}$	$0.0^{+7.8}_{-0.0}$	$0.0^{+0.0}_{-0.0}$	$0.2^{+1.2}_{-0.2}$	$2.2^{+0.2}_{-0.5}$
Dolag	SIBYLL	4.41	$2.29^{+0.06}_{-0.79}$	$19.74^{+0.00}_{-0.40}$	$84.3^{+5.2}_{-11.9}$	$0.0^{+85.6}_{-0.0}$	$84.3^{+0.0}_{-84.3}$	$0.0^{+16.6}_{-0.0}$	$2.5^{+10.5}_{-2.4}$	$13.2^{+0.0}_{-12.1}$
	EPOS	4.74	$2.23^{+0.11}_{-0.06}$	$19.75^{+0.03}_{-0.29}$	$90.8^{+3.7}_{-3.8}$	$0.0^{+87.9}_{-0.0}$	$90.8^{+0.0}_{-90.0}$	$0.0^{+0.0}_{-0.0}$	$0.0^{+5.8}_{-0.0}$	$9.2^{+0.0}_{-5.2}$
	QGS4	6.28	$2.23^{+0.08}_{-0.09}$	$19.64^{+0.10}_{-0.12}$	$97.1^{+0.4}_{-1.0}$	$54.4^{+28.3}_{-35.4}$	$42.7^{+34.7}_{-28.4}$	$0.0^{+0.0}_{-0.0}$	$0.0^{+0.0}_{-0.0}$	$2.9^{+0.9}_{-0.5}$
CLUES	SIBYLL	1.76	$2.54^{+0.00}_{-0.19}$	$19.45^{+0.50}_{-0.12}$	$91.8^{+0.3}_{-11.4}$	$74.5^{+8.5}_{-74.5}$	$17.3^{+66.2}_{-10.8}$	$0.0^{+0.0}_{-0.0}$	$0.0^{+9.2}_{-0.0}$	$8.2^{+3.5}_{-1.8}$
	EPOS	1.87	$2.43^{+0.06}_{-0.13}$	$19.51^{+0.36}_{-0.07}$	$94.4^{+0.4}_{-4.4}$	$68.6^{+14.1}_{-68.6}$	$25.8^{+64.4}_{-13.4}$	$0.0^{+0.0}_{-0.0}$	$0.0^{+3.5}_{-0.0}$	$5.6^{+2.5}_{-0.9}$
	QGS4	3.10	$2.32^{+0.08}_{-0.05}$	$19.56^{+0.08}_{-0.07}$	$97.4^{+0.4}_{-0.5}$	$68.8^{+16.3}_{-15.8}$	$28.6^{+15.6}_{-16.1}$	$0.0^{+0.0}_{-0.0}$	$0.0^{+0.0}_{-0.0}$	$2.6^{+0.5}_{-0.4}$
Rand.A	SIBYLL	2.84	$2.40^{+0.07}_{-0.11}$	$19.86^{+0.12}_{-0.18}$	$69.3^{+11.1}_{-19.2}$	$0.0^{+43.1}_{-0.0}$	$69.3^{+8.3}_{-54.4}$	$24.5^{+19.2}_{-12.3}$	$1.3^{+3.0}_{-1.3}$	$4.9^{+1.0}_{-1.4}$
	EPOS	2.15	$2.34^{+0.08}_{-0.09}$	$19.69^{+0.19}_{-0.08}$	$87.6^{+5.6}_{-4.2}$	$38.0^{+23.3}_{-38.0}$	$49.6^{+34.2}_{-23.5}$	$9.5^{+3.5}_{-7.3}$	$0.3^{+1.8}_{-0.3}$	$2.6^{+0.9}_{-0.5}$
	QGS4	2.51	$2.23^{+0.07}_{-0.07}$	$19.58^{+0.07}_{-0.08}$	$98.9^{+0.0}_{-3.5}$	$57.9^{+18.4}_{-12.1}$	$41.0^{+10.0}_{-20.7}$	$0.0^{+3.5}_{-0.0}$	$0.0^{+0.1}_{-0.0}$	$1.1^{+0.2}_{-0.2}$
Rand.B	SIBYLL	2.57	$2.47^{+0.04}_{-0.16}$	$19.71^{+1.40}_{-0.08}$	$58.4^{+10.5}_{-23.6}$	$48.3^{+5.3}_{-48.3}$	$10.1^{+41.8}_{-10.1}$	$38.8^{+22.2}_{-13.4}$	$0.0^{+3.5}_{-0.0}$	$2.8^{+1.6}_{-0.4}$
	EPOS	2.29	$2.33^{+0.09}_{-0.15}$	$19.60^{+0.23}_{-0.09}$	$79.5^{+5.8}_{-6.5}$	$57.7^{+20.2}_{-37.2}$	$21.8^{+34.9}_{-21.8}$	$18.2^{+5.8}_{-6.3}$	$0.7^{+1.9}_{-0.7}$	$1.6^{+0.7}_{-0.4}$
	QGS4	2.60	$1.97^{+0.26}_{-0.05}$	$19.52^{+0.08}_{-0.07}$	$95.8^{+1.7}_{-4.5}$	$45.6^{+41.0}_{-9.4}$	$50.2^{+9.0}_{-43.1}$	$2.2^{+5.1}_{-2.2}$	$0.9^{+0.6}_{-0.9}$	$1.1^{+0.2}_{-0.4}$

Table 1: Constant fraction fit energy spectrum parameters and nuclei emission percentages.

Magnetic field strength significantly influences elemental fractions, with nitrogen increasing with higher fields while silicon and iron decrease. Compared to previous FR0 fits ($z \leq 0.05$) [17], helium fractions have increased for QGSJetII-04 and EPOS-LHC (except no-field), while protons have decreased. Nitrogen has increased for Rand.A-EPOS and Rand.B-EPOS but decreased for Rand.A-QGS4 and Rand.B-QGS4. Silicon remains negligible across all configurations.

Excluding disfavored configurations, best-fit elemental fraction (%) ranges are: $58.4 \leq f_{\text{H}} + f_{\text{He}} \leq 98.9$, $0.0 \leq f_{\text{H}} \leq 74.5$, $10.1 \leq f_{\text{He}} \leq 69.3$, $0.0 \leq f_{\text{N}} \leq 38.8$, $0.0 \leq f_{\text{Si}} \leq 1.3$, $1.1 \leq f_{\text{Fe}} \leq 8.2$.

4.1.3 Multi-messenger Photons and Neutrinos

Cosmogenic integral photon and all-flavor neutrino spectra for the best-fit CLUES-SIBYLL configuration are shown in Fig. 2(top), compared to the no-field case. Despite SIBYLL reconstruct-

ing a heavier mass than other models, it predicts 92% light-nuclei emission from FR0s propagated through CLUES. At low energies, photon flux matches a pure proton cosmogenic model, while at higher energies, it shifts toward mixed composition predictions.

Neutrino flux resembles pure iron sources, potentially due to the simulation's restriction to nearby FR0s ($z \leq 0.2$). Compared to previous FR0 fits ($z \leq 0.05$), high-energy neutrinos are slightly reduced, but differences are minor [17]. Flux predictions remain within theoretical ranges and experimental limits.

Intergalactic magnetic fields generally increase photon and neutrino fluxes, especially at high energies (Fig. 2, bottom). Photon flux strongly correlates with proton fraction—No-Field-EPOS, with 93.5% protons, has the highest flux, while Rand.A-SIBYLL, with 0% protons, has the lowest. Without a magnetic field, iron produces 55 times fewer photons than protons, as photopion interactions are less efficient. Magnetic fields enhance photon detection by increasing interaction paths. In the Rand.B 1nG-3Mpc field, a proton source emits ~ 3 times more photons than the no-field case.

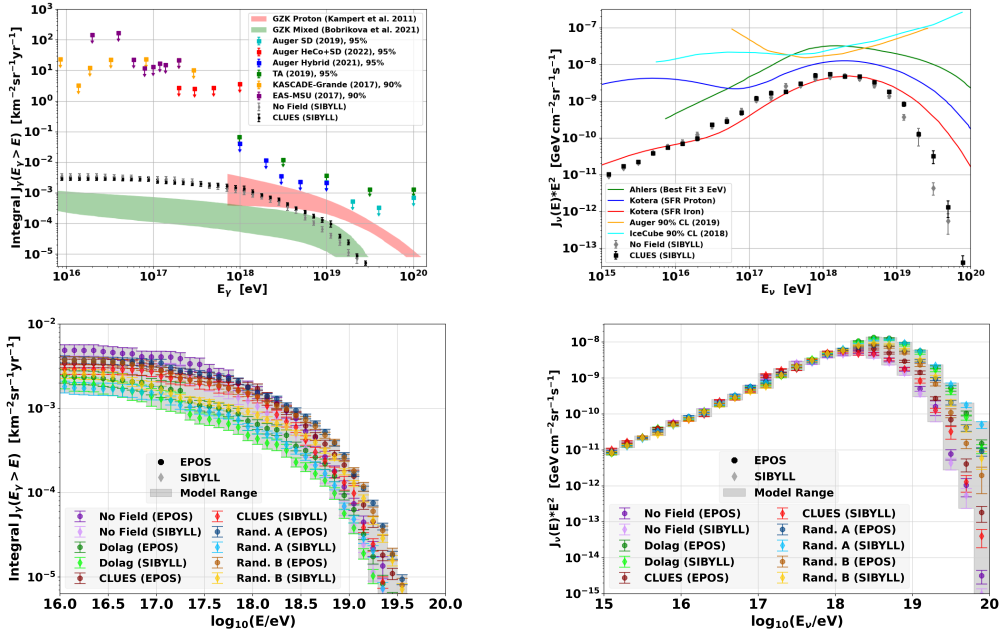


Figure 2: Constant fraction fits cosmogenic photon (left) and neutrino (right) spectra. Top: Best-fit (CLUES-SIBYLL) and no-field cases with models and upper limits [19–22]. Bottom: Results for all fits.

Neutrino flux increases with magnetic fields—Rand.B 1nG-3Mpc yields 1.6 times more neutrinos than no-field for iron, while protons show a smaller increase (1.03x). Unlike photons, neutrino production scales with mass number, with iron producing 1.3 times more neutrinos than protons in the no-field case.

In summary, intergalactic magnetic fields enhance cosmogenic photon and neutrino production. However, fitted compositions and spectra influence fluxes: softer spectra and strong cutoffs (e.g., no-field) result in fewer high-energy photons and neutrinos.

4.2 Evolving Fraction Fits

The evolving fraction fit results for all five magnetic field models and two EAS models (EPOS-LHC and Sibyll2.3c) are shown in [8]. The QGSJetII-04 model was excluded from this analysis.

Forty-four nuclei fractions result in nearly perfect $\langle \ln A \rangle$ fits across all configurations due to the large number of parameters. Similar to the constant fraction fits, 1 nG random fields best match the lower-energy $\langle \ln A \rangle$ bins and provide the best fits to the highest energy bins of the energy spectrum, with Rand.B consistently performing the best. All models except Rand.B underfit the highest energy bin, with the CLUES model again showing the largest discrepancy.

4.2.1 Energy Spectrum Parameters

Table 2 summarizes the best-fit spectral parameters. As with constant fraction fits, higher $\langle B \rangle$ and B_{RMS} generally lead to steeper spectral indices (γ) and higher cutoff rigidities (R_{cut}), except for Rand.B, where this trend reverses. The trajectory cutoff (D_{cut}) remains stable except for the high- B_{RMS} Dolag field.

Rand.B provides the best overall fit, followed closely by CLUES. EPOS-LHC is favored except in Rand.B, where Sibyll2.3c performs slightly better. The bounds of best-fit parameters, including all configurations, are: $1.94 \leq \gamma \leq 2.65$, $19.19 \leq \log_{10}(R_{\text{cut}}/V) \leq 19.95$, $841 \leq D_{\text{cut}}/\text{Mpc} \leq 907$, and $1.328 \leq n \leq 1.346$. These ranges are larger than the constant fraction fits, as the weak-field cases are included.

Field	Model	$\Sigma\chi^2/\text{bin}$	γ	$\log_{10}(R_{\text{cut}}/V)$	$D_{\text{cut}}/\text{Mpc}$	n
No Field	SIBYLL	0.370	$2.10^{+0.47}_{-0.14}$	$19.19^{+0.84}_{-0.20}$	844^{+0}_{-1}	$1.344^{+0.014}_{-0.005}$
	EPOS	0.326	$1.94^{+0.60}_{-0}$	$19.22^{+0.75}_{-0.01}$	844^{+0}_{-1}	$1.343^{+0.006}_{-0.005}$
Dolag	SIBYLL	0.469	$2.28^{+0.14}_{-0.84}$	$19.89^{+0.31}_{-0.98}$	907^{+450}_{-50}	$1.328^{+0.023}_{-0.000}$
	EPOS	0.446	$2.31^{+0.12}_{-0.20}$	$19.89^{+0.40}_{-0.38}$	889^{+146}_{-39}	$1.342^{+0.006}_{-0.011}$
CLUES	SIBYLL	0.307	$2.65^{+0.00}_{-0.29}$	$19.58^{+0.27}_{-0.25}$	841^{+1}_{-0}	$1.342^{+0.013}_{-0.007}$
	EPOS	0.295	$2.52^{+0.09}_{-0.22}$	$19.58^{+0.51}_{-0.20}$	842^{+0}_{-1}	$1.342^{+0.006}_{-0.004}$
Rand.A	SIBYLL	0.344	$2.64^{+0.20}_{-0.25}$	$19.95^{+0.50}_{-0.56}$	855^{+93}_{-7}	$1.343^{+0.008}_{-0.005}$
	EPOS	0.341	$2.65^{+0.05}_{-0.30}$	$19.89^{+0.94}_{-0.32}$	844^{+113}_{-0}	$1.342^{+0.006}_{-0.006}$
Rand.B	SIBYLL	0.236	$2.35^{+0.34}_{-0.30}$	$19.40^{+1.64}_{-0.32}$	843^{+171}_{-0}	$1.346^{+0.009}_{-0.006}$
	EPOS	0.237	$2.21^{+0.34}_{-0.45}$	$19.51^{+1.20}_{-0.38}$	843^{+174}_{-0}	$1.342^{+0.004}_{-0.007}$

Table 2: Evolving fraction fits energy spectrum parameters.

4.2.2 UHECR Composition Parameters

Fig. 3 shows the best-fit emission fractions as a function of energy. Proton and helium exhibit instability due to propagation effects, while their combined fraction is more stable. Emitted proton fraction increases above 10^{19} eV. Magnetic field strength impacts composition, increasing nitrogen while decreasing silicon and iron. The energy bin averaged best-fit elemental fractions (%) are: $63.3 \leq f_{\text{H}} + f_{\text{He}} \leq 95.0$, $21.8 \leq f_{\text{H}} \leq 60.7$, $27.0 \leq f_{\text{He}} \leq 52.6$, $2.9 \leq f_{\text{N}} \leq 28.4$, $1.1 \leq f_{\text{Si}} \leq 10.5$, $0.6 \leq f_{\text{Fe}} \leq 6.4$. Iron contributes minimally in all cases.

4.2.3 Multi-messenger Photons and Neutrinos

The evolving fraction fit predictions for cosmogenic integral photon and all-flavor neutrino spectra are shown in Figure 4. The top plots include the best-fit Rand.B-SIBYLL configuration compared to the no-field scenario and models with experimental upper limits.

Despite SIBYLL reconstructing a heavier mass composition, the evolving fraction fit still predicts that $\sim 66\%$ of the FR0 emission consists of light nuclei. At lower energies ($E_{\gamma} \leq 10^{17}$ eV),

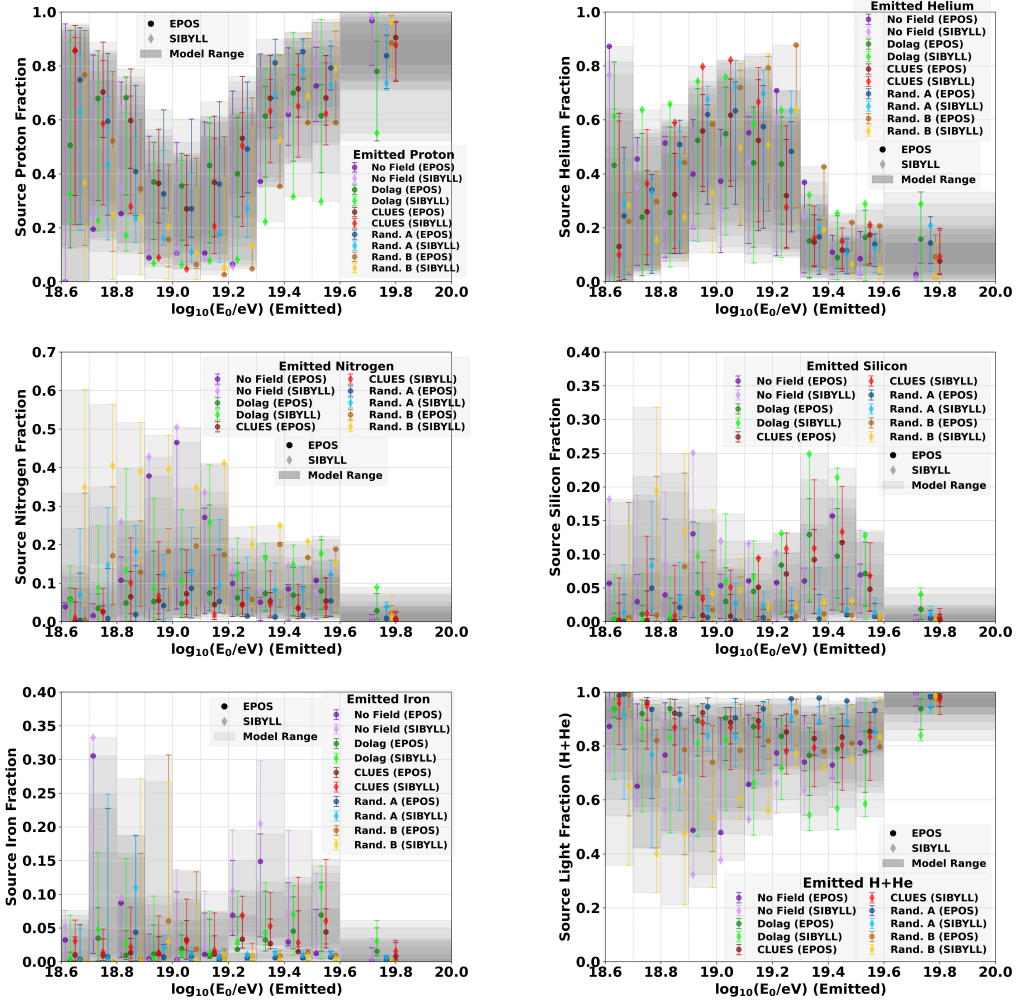


Figure 3: Evolving fraction fit emitted nuclei fractions for all configurations. The last panel shows the combined proton and helium fraction. Grey bands indicate $\pm 1\sigma$ and darken where overlapping.

the photon flux remains consistent with a pure proton source, shifting toward a mixed composition at higher energies. The neutrino flux resembles a pure iron source, possibly due to the simulation constraint of $z \leq 0.2$ for FR0s. Across all configurations, magnetic fields increase the flux of both photons and neutrinos, with the effect being most significant at the highest energies, as shown in Figure 4 (bottom).

5. Summary & Conclusions

This study explored FR0 radio galaxies as UHECR sources, leveraging their high abundance despite their lower individual luminosities. Using CRPropa3 [9], we simulated isotropic UHECR emissions based on FR0 properties and fit the results to Pierre Auger Observatory data [12, 13].

The combined fits across two fit models, three EAS models, and five magnetic field configurations demonstrate that FR0s can largely account for the observed UHECR spectrum and composition. These findings, along with prior studies [3], support FR0s as viable UHECR sources. Additionally, secondary photon and neutrino fluxes remain within observational limits, highlighting the potential for future multi-messenger constraints.

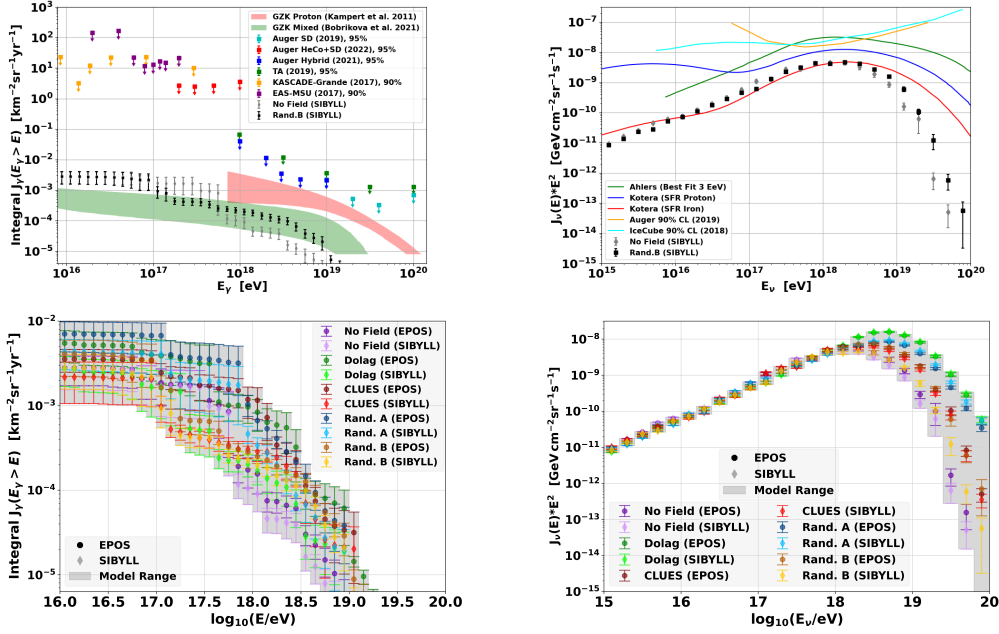


Figure 4: Evolving fraction fits cosmogenic photon (left) and neutrino (right) spectra. Top: Best-fit (Rand.B-SIBYLL) and no-field cases with models and upper limits [19–22]. Bottom: Results for all fits.

At the highest energies, some tested configurations underpredict flux and all models underpredicted $\langle \ln A \rangle$, suggesting a possible contribution from alternative heavier average nuclei sources. The influence of IGMFs is critical, affecting composition, energy spectra, and secondary messengers. Stronger fields favor heavier nuclei emission and harder spectra ($\langle \gamma \rangle \approx 2.4$), while increasing high-energy secondary photon and neutrino fluxes. The CLUES magnetic field model [11] provides the best fit for constant fractions, consistent with estimates from cosmic ray multiplets [23].

In summary, FR0 galaxies emerge as plausible contributors to the observed UHECR flux. This study refines our understanding of UHECR sources and provides a foundation for future multi-messenger astrophysics investigations.

Acknowledgments: Financial support received from the grant numbers I 4144-N27 (FWF), N1-0111 (ARRS), SFB1491 (DFG), 847476 (EU). Further information is in Ref. [8].

References

- [1] A. Aab, et al., NIMA 798 (2015) 172–213.
- [2] R. D. Baldi, et al., A&A 609 (2018) A1.
- [3] L. Merten, et al., ApP 128 (2021) 102564.
- [4] A. M. Hillas, ARA&A 22 (1984) 425–444.
- [5] P. Bhattacharjee, G. Sigl, PR 327 (2000) 109.
- [6] M. Boughelilba, A. Reimer, ApJ 955 (2) (2023) L41.
- [7] N. S. Khatiya, et al., ApJ 971 (1) (2024) 84.
- [8] J. P. Lundquist, et al., ApJ 978 (1) (2025) 20.
- [9] R. Alves Batista, et al., JCAP 09 (2022) 035.
- [10] K. Dolag, et al., JCAP 01 (2005) 009.
- [11] S. Hackstein, et al., MNRAS 475 (2) (2018) 2519.
- [12] A. Yushkov, PoS ICRC2019 (2020) 482.
- [13] O. Deligny, PoS ICRC2019 (2020) 234.
- [14] A. Abdul Halim, et al., JCAP 07 (2024) 094.
- [15] A. Abdul Halim, et al., PRD 109 (2024) 102001.
- [16] P. Virtanen, et al., Nat. Meth. 17 (2020) 261.
- [17] J. P. Lundquist, et al., PoS ICRC2023 (2023) 1512.
- [18] A. Aab, et al., JCAP 04 (2017) 038.
- [19] P. Abreu, et al., ApJ 933 (2) (2022) 125.
- [20] M. G. Aartsen, et al., PRD 98 (6) (2018) 062003.
- [21] A. Aab, et al., JCAP 10 (2019) 022.
- [22] K. Kotera, et al., JCAP 2010 (10) (2010) 013.
- [23] R. U. Abbasi, et al., ApJ 899 (1) (2020) 86.